Evidence of stress relaxation caused by time-dependent deformation in the damage zone of the Chelungpu fault system

Mayukh Talukdar[1] and Hiroki Sone[1]

[1]University of Wisconsin-Madison

September 11, 2023

Abstract

High fracture density in fault damage zones not only reduces the elastic stiffness of rocks but may also promote time-dependent bulk deformation through the sliding of fracture surfaces and thus impact the stress evolution in fault zones. Comparing the damage zones of the three faults in the Chelungpu fault system encountered in the Taiwan Chelungpu fault Drilling Project (TCDP), the youngest damage zone showed pronounced sonic velocity reduction even though fracture density is the same for all three fault zones, consistent with the shorter healing time of the youngest fault. Caliper log data showed a time-dependent enlargement of the borehole wall at the damage zone. These damage zones record lower differential stress than the surrounding host rock, which cannot be explained by the reduced elastic stiffness in the damage zone. Stress relaxation caused by time-dependent bulk deformation in the damage zone may be responsible for the observed low differential stress.

Hosted file

973052_0_art_file_11354858_s0k9jw.docx available at https://authorea.com/users/660240/articles/663876-evidence-of-stress-relaxation-caused-by-time-dependent-deformation-in-the-damage-zone-of-the-chelungpu-fault-system

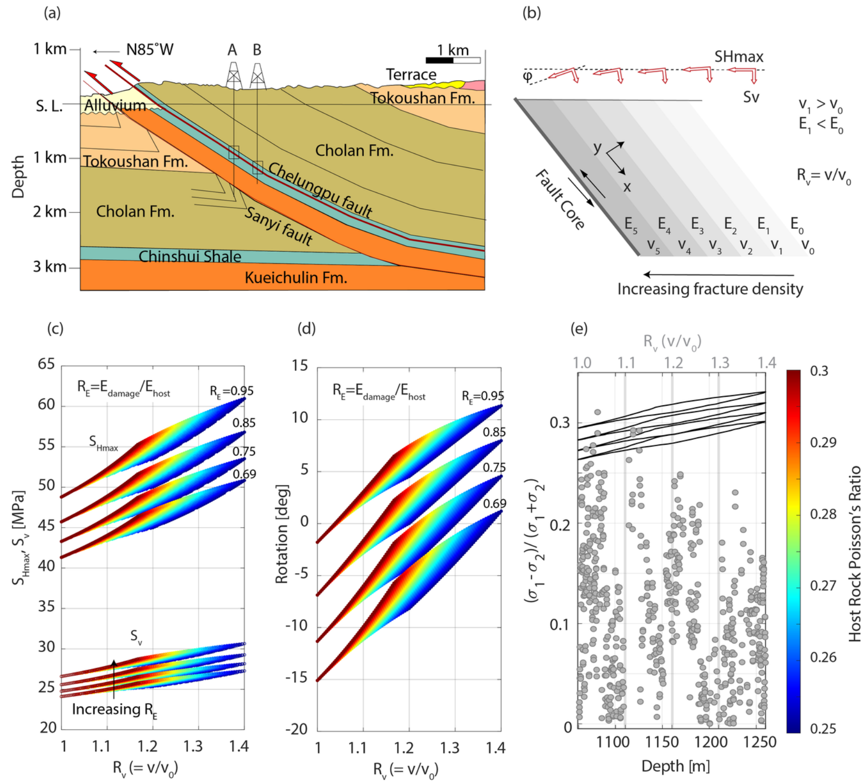
(a)
1 km
N85°W
A
B
1 km
Terrace
S. L.
Alluvium
Tokoushan Fm.
Depth
1 km
2 km
3 km
Tokoushan Fm.
Cholan Fm.
Cholan Fm.
Chelungpu fault
Sanyi fault
Chinshui Shale
Kueichulin Fm.
(b)
SHmax
Sv
φ
$v_1 > v_0$
$E_1 < E_0$
$R_v = v/v_0$
y
x
Fault Core
E_5 E_4 E_3 E_2 E_1 E_0
v_5 v_4 v_3 v_2 v_1 v_0
Increasing fracture density
(c)
$R_E=E_{damage}/E_{host}$
R_E=0.95
0.85
0.75
0.69
S_{Hmax}
S_v
Increasing R_E
S_{Hmax}, S_v [MPa]
R_v (= v/v_0)
(d)
$R_E=E_{damage}/E_{host}$
R_E=0.95
0.85
0.75
0.69
Rotation [deg]
R_v (= v/v_0)
(e)
R_v (v/v_0)
$(\sigma_1-\sigma_2)/(\sigma_1+\sigma_2)$
Depth [m]
Host Rock Poisson's Ratio

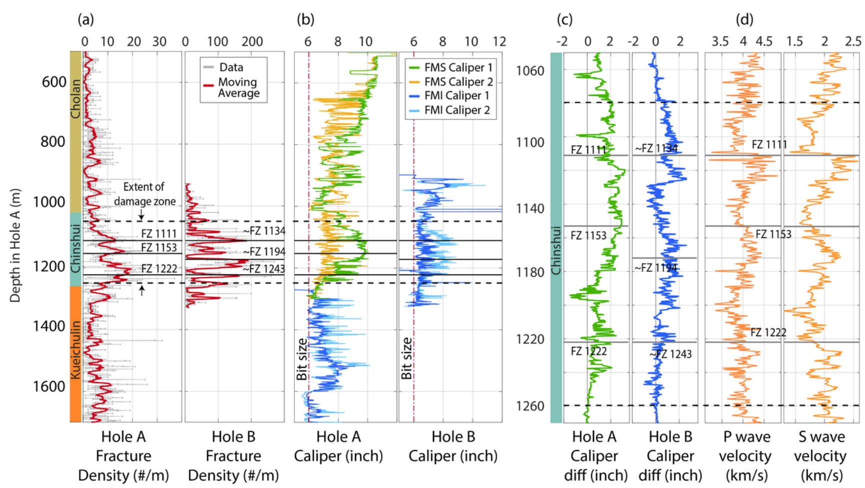
(a)
(b)
(c)
(d)
Data
Moving Average
Cholan
Chinshui
Kueichulin
Extent of damage zone
FZ 1111
FZ 1153
FZ 1222
~FZ 1134
~FZ 1194
~FZ 1243
Depth in Hole A (m)
FMS Caliper 1
FMS Caliper 2
FMI Caliper 1
FMI Caliper 2
Bit size
Bit size
Chinshui
Hole A Fracture Density (#/m)
Hole B Fracture Density (#/m)
Hole A Caliper (inch)
Hole B Caliper (inch)
Hole A Caliper diff (inch)
Hole B Caliper diff (inch)
P wave velocity (km/s)
S wave velocity (km/s)

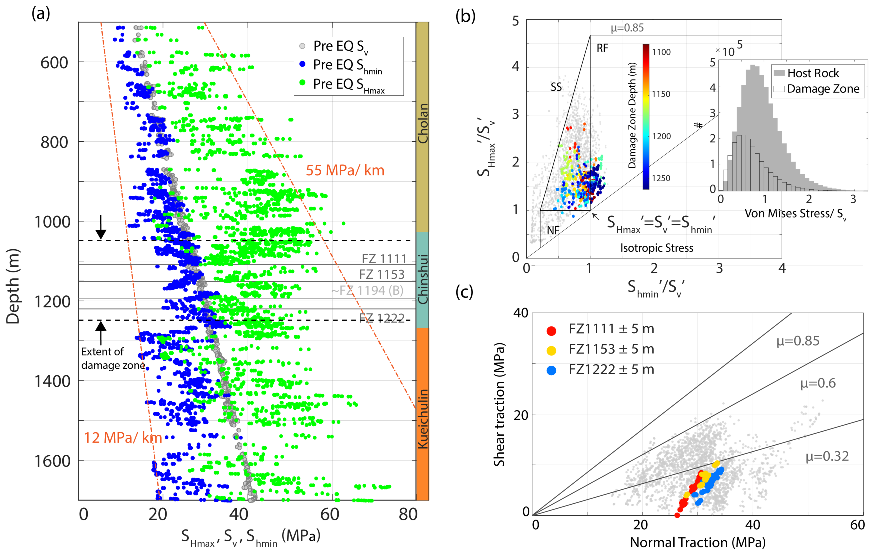

(a)
Pre EQ S_v
Pre EQ S_{hmin}
Pre EQ S_{Hmax}
55 MPa/ km
12 MPa/ km
FZ 1111
FZ 1153
~FZ 1194 (B)
FZ 1222
Extent of damage zone
Cholan
Chinshui
Kueichulin
Depth (m)
S_{Hmax}, S_v, S_{hmin} (MPa)
(b)
μ=0.85
RF
SS
NF
Damage Zone Depth (m)
Host Rock
Damage Zone
Von Mises Stress/ S_v
$S_{Hmax}'=S_v'=S_{hmin}'$
Isotropic Stress
S_{Hmax}'/S_v'
S_{hmin}'/S_v'
(c)
FZ1111 ± 5 m
FZ1153 ± 5 m
FZ1222 ± 5 m
μ=0.85
μ=0.6
μ=0.32
Shear traction (MPa)
Normal Traction (MPa)

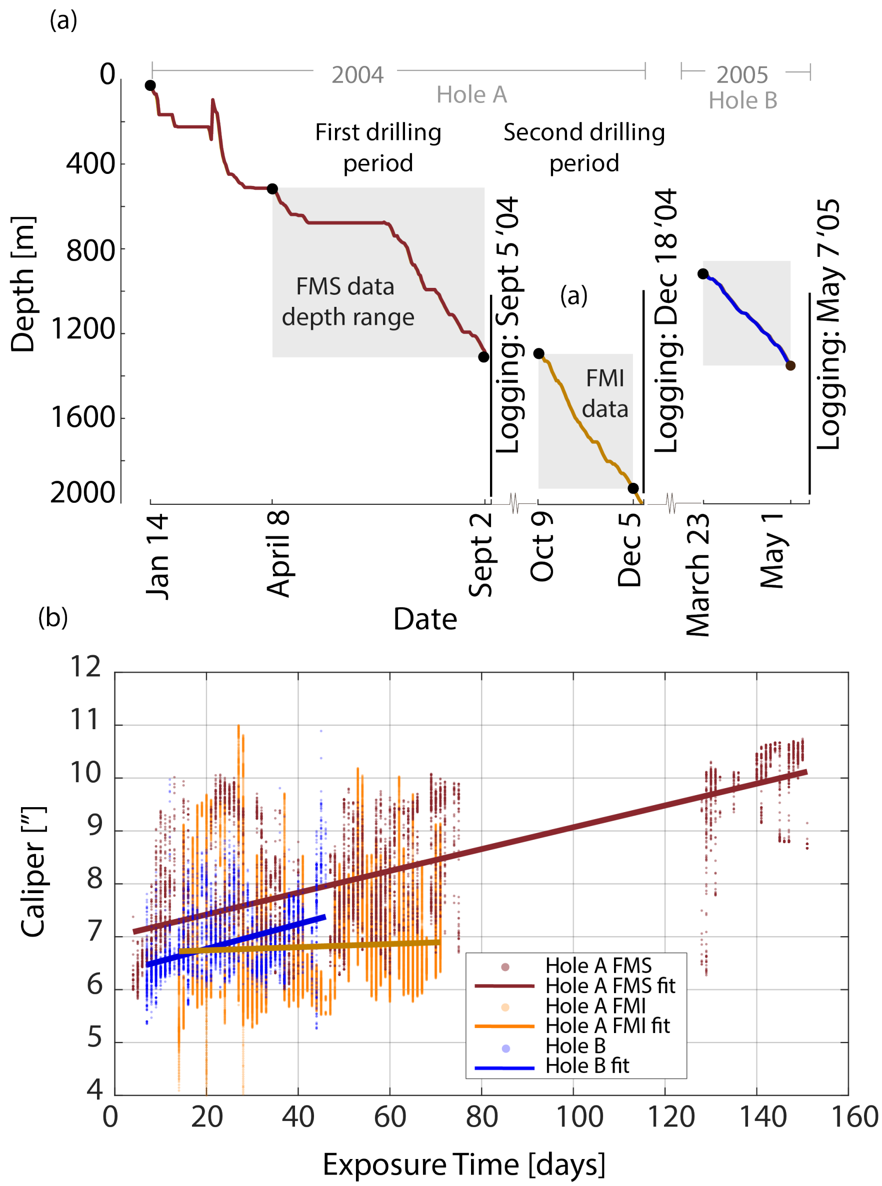
(a)
2004
Hole A
2005
Hole B
First drilling period
Second drilling period
FMS data depth range
FMI data
Logging: Sept 5 ’04
Logging: Dec 18 ’04
Logging: May 7 ’05
Depth [m]
0
400
800
1200
1600
2000
Jan 14
April 8
Sept 2
Oct 9
Dec 5
March 23
May 1
Date
(b)
Caliper ["]
Exposure Time [days]
Hole A FMS
Hole A FMS fit
Hole A FMI
Hole A FMI fit
Hole B
Hole B fit

Evidence of stress relaxation caused by time-dependent deformation in the damage zone of the Chelungpu fault system

Mayukh Talukdar[1], Hiroki Sone[1]

[1] Department of Civil and Environmental Engineering, Geological Engineering Program, University of Wisconsin-Madison

Corresponding author: Mayukh Talukdar (mtalukdar@wisc.edu)

Key Points:

- The damage zones are characterized by sections of high fracture density resulting in borehole enlargement and low sonic velocity
- Time-dependent borehole enlargement and healing implies the occurrence of bulk viscous deformation in the damage zone
- Viscous stress relaxation may be responsible for the relatively isotropic stress state in the damage zone prior to the Chi-Chi earthquake

Abstract

High fracture density in fault damage zones not only reduces the elastic stiffness of rocks but may also promote time-dependent bulk deformation through the sliding of fracture surfaces and thus impact the stress evolution in fault zones. Comparing the damage zones of the three faults in the Chelungpu fault system encountered in the Taiwan Chelungpu fault Drilling Project (TCDP), the youngest damage zone showed pronounced sonic velocity reduction even though fracture density is the same for all three fault zones, consistent with the shorter healing time of the youngest fault. Caliper log data showed a time-dependent enlargement of the borehole wall at the damage zone. These damage zones record lower differential stress than the surrounding host rock, which cannot be explained by the reduced elastic stiffness in the damage zone. Stress relaxation caused by time-dependent bulk deformation in the damage zone may be responsible for the observed low differential stress.

Plain Language Summary

Earthquakes occur along large faults in the earth's crust. The region surrounding a fault hosts a dense network of fractures and slip surfaces, along which deformation occurs. In this study, we show evidence of time-dependent healing and deformation of off-fault rocks, which potentially modified stress on faults during the interseismic period and therefore has implications for seismic risk and hazard assessment. Mechanical waves passing through young fault damage zone are slower than waves passing through old damage zones in the Chelungpu fault system, suggesting a temporal process governing the healing of faults. We observe that the shear stress magnitude is lower in the fault damage zone than in the intact host rock. Because elastic properties of damage zone rocks cannot explain the low shear stress, we suggest that other processes like time-dependent bulk deformation relax the stress in fault damage zones.

1 Introduction

A fault system is broadly comprised of a fault core, flanking damage zone, and surrounding host rock. The fault core is a narrow, commonly mms-cms wide zone that accommodates motion by localized slip during aseismic creep, and/or earthquakes (Chester et al., 1993; Scholz, 2019; Shipton and Cowie, 2001; Sibson, 2003). The surrounding fault damage zone is characterized by high fracture density (Chester and Logan, 1986), which lowers the stiffness of fault damage zone rocks (Faulkner et al., 2006; Griffith et al., 2009) compared to the host rock. Such compliant damage zones can cause enhanced interseismic shear strain rates as observed in geodetic studies, for instance along the San Andreas and San Jacinto faults (Lindsey et al., 2014; Materna and Bürgmann, 2016).

Off-fault strain accumulation has been inferred from the discrepancy between geologic, geodetic, and modeled slip rates. Kinematic models by Bird (2009) suggested that 1/3rd of the plate motion along the Pacific-North American plate boundary in California occurs as permanent distributed off-fault deformation. Johnson (2013) also showed that kinematic models fit geodetic velocities better in Southern California when intra-block deformation was allowed, and such off-fault strain rates may constitute 28-33% of the total geodetic moment rate. InSAR-derived surface displacements have also documented slip deficits on faults during shallow earthquakes: Bam, Izmit, Hector Mine, and Landers earthquakes (Fialko, 2006). The remainder of the slip has been attributed to inelastic and distributed off-fault deformation during the inter-seismic period (Fialko, 2006). These observations indicate that damage zone deformation may be taking place either in small hidden faults or as distributed rock deformation.

Since deformation may concentrate in damage zones and evidence of off-fault strain accumulation is found from various geodetic observations, we suggest that a substantial amount of interseismic off-fault deformation is accommodated in damage zones even where the fault plane itself is partial to fully locked. Damage zones likely deform by progressive sliding of fracture surfaces and time-dependent closure of fracture surfaces during the interseismic period (Meyer et al., 2021; Sone and Condon, 2017). Such off-fault strain accumulation in fault damage zones may progressively alter the damage zone stress state and in turn alter the shear stress magnitude on the fault plane (Sone and Uchide, 2016). We suggest that in the presence of a viscous damage zone with finite thickness, time-dependent distributed deformation can lead to the relaxation of the shear stress that would otherwise accumulate on a locked fault during the interseismic period.

In this paper, we report potential evidence of time-dependent off-fault deformation in the Chelungpu fault system that ruptured during the Mw 7.3, 1999 Chi-Chi earthquake in Taiwan. We derive evidence from well logs and cores drilled across the Chelungpu fault system. We further argue that the low differential stress around the fault zone reflects the time-dependent plastic deformation and associated stress relaxation occurring in the damage zone.

2 Materials and Methods

Boreholes from the Taiwan Chelungpu fault Drilling Project (TCDP) are suitable for this study because they cut fault zones that are likely of different ages, i.e., different amounts of time since the last rupture. Moreover, cores with >90% recovery rate, high quality log data, and abundant existing literature provide rich information about the rock type, rock properties, and structures encountered in the Chelungpu fault system. The rock types in this area range from sand-rich to silt-rich sedimentary rocks, with intermediate lithologies like sandy siltstone, silty sandstone, and bioturbated siltstone.

We characterized the damage zone in the Chelungpu fault system with the aid of geophysical logs including caliper and sonic logs. Caliper logs provide continuous measures of borehole diameter with depth. In TCDP, four arm calipers were used where two caliper readings from perpendicular arm pairs are averaged to provide borehole diameter information. Differences between the drill bit size (6 inches) and caliper readings is an indication that the borehole diameter increased due to rock failure at the borehole wall. Formation P-wave and S-wave velocities were also collected from sonic logs (Wu et al., 2008; Hung et al., 2009).

The in-situ state of stress along the TCDP borehole was determined in Talukdar et al. (2022) by integrating borehole failure observations, laboratory experiments, log data and hydraulic fracturing stress measurements. They observed that both the occurrence of borehole failures and rock strengths were dependent on lithology, underlining a lithological control on in-situ stress magnitude. They also used the correlation between gamma ray log and minimum principal stress determined by previous studies to estimate a profile of minimum horizontal principal stress (S_{hmin}). The compressive strength profile, breakout width, and the estimated S_{hmin} profile were combined to calculate the maximum horizontal principal stress (S_{Hmax}). Using an edge dislocation model, they calculated the coseismic stress change during the Chi-Chi earthquake, which was then subtracted from the post-earthquake in-situ stress profile determined above to estimate the pre-earthquake principal stress magnitudes (details in Talukdar et al., 2022).

3 Results

3.1 Depth range of damage zone

The Taiwan Chelungpu Drilling Project (TCDP) encountered three large faults in each borehole (Yeh et al., 2007; Sone et al., 2007). Hole A encountered faults at 1111, 1153, and 1222 m depths as shown by the black horizontal lines in Figure 1a. Hole B was drilled further away from the fault surface rupture (Figure 4a), therefore, encountering the same faults at deeper depths at 1134, 1194 and 1243 m (Hirono et al., 2007).

We counted visible fractures on fresh wet cores from Hole A (recovered within hours) and dried stored cores from Hole B (13 years after recovery) to characterize fracture density, i.e., the number of fractures per meter of core (Figure 1a). Fracture densities were higher in Hole B likely because of the fractures that opened upon drying. The fracture count increases in the Chinshui Shale especially in the proximity to the 3 faults (Figure 1a). Thus, from the depth range where the fracture count is higher, the damage zone of the Chelungpu fault system is suggested to lie between 1080-1260 m.

We also observe an increase in one of the caliper readings at the damage zone in both boreholes (Figure 1b), which is caused by breakout growth in the fault damage zone (Plumb and Hickman, 1985). A similar observation has been made by Sahara et al. (2014), where borehole breakouts deepen and expand in regions of high fracture density, leading to a preferential increase in caliper reading in the direction of the breakout. Such an increase in one caliper reading extends from 1080-1260 m, where we suggest rock strength is compromised due to the increase in fracture density in the damage zone (Figure 1a), thus leading to frequent occurrence of breakouts.

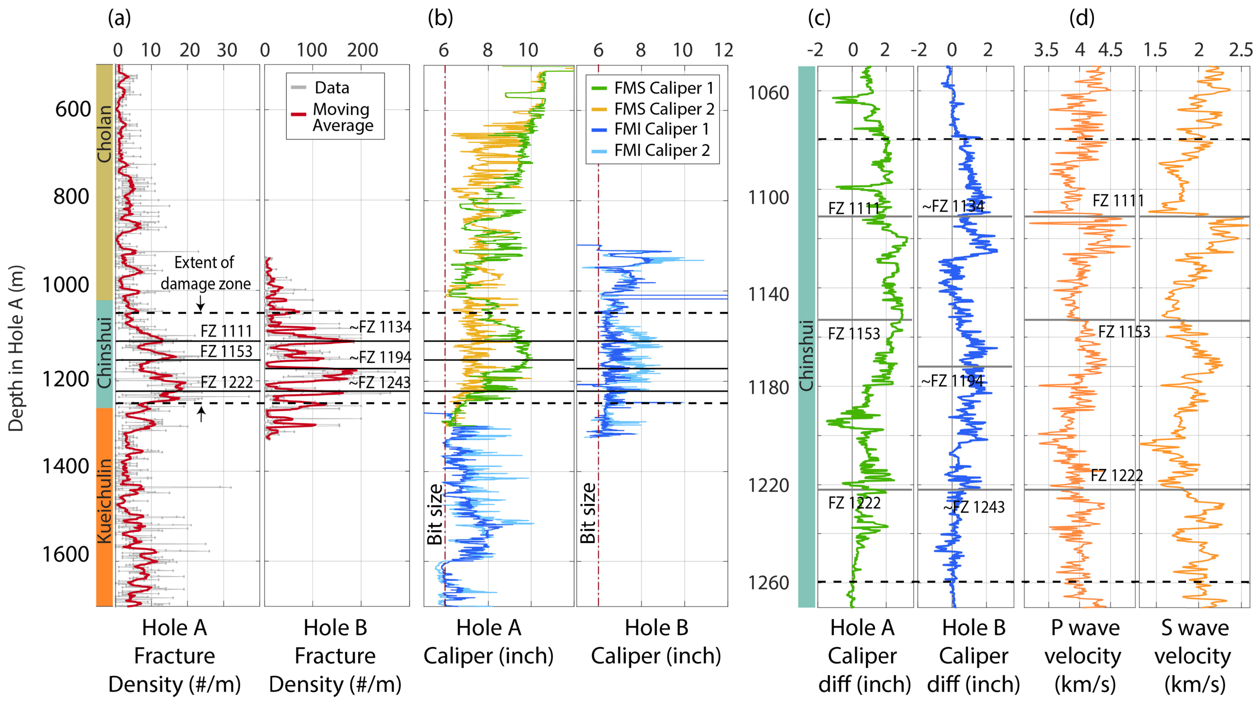

Figure 1. Data sets showing the extent of damage zones between dashed lines (1080-1260 m). Hole B log depths are shifted up by 22 m for comparison with Hole A data based on the lithology depth shift found in Talukdar et al. (2022). **a)** Fracture density profile observed from drilled cores (lithological column from Song et al., 2007). **b)** Caliper data. The difference in calipers 1 and 2 indicates borehole enlargement at the fault damage zone. **c)** Difference between caliper readings for Hole A and B near the damage zone. **d)** P- and S- wave velocity from Hole A sonic log near the damage zone.

3.2 Comparison between individual fault damage zones

While the entire depth range from 1080-1260 m shows high fracture density and higher caliper difference, we observe local decreases in sonic velocity at or above the 3 fault planes. We also observe that the caliper reading difference is greater within ±20 m of the fault plane, especially noticeable in the Hole B data. Thus, within the ~200 m broad fault damage zone, there are individual damage zones associated with each fault plane with an even higher degree of damage.

We observe that sonic velocity reduction is most prominent for the shallowest fault and less prominent in the deeper faults (Figure 1d). Likewise, if we compare the difference in caliper readings for the three fault zones in Figure 1c, the shallowest fault shows the highest difference between readings, but the difference in caliper readings is less for the deeper faults. The fracture density, however, is similar in all three fault zones (Figure 1a). These are interpreted later in relation to the age of the faults.

3.3 Time-dependent borehole enlargement

Hole A logging took place during two drilling periods as shown in Figure 2a. The first period involved drilling from the surface down to 1300 m below the surface. The second drilling period cut from 1300-2000 m. After each drilling period, logging data were collected. From the drilling record, exposure time is calculated which describes how long the borehole was exposed from the day of drill bit penetration to the day of logging. Within each run, exposure time at the top of the borehole is longer than at the bottom because drilling is completed from top to bottom followed by logging.

Figure 2b shows that caliper measurements increase with exposure time during each run. The time-dependent borehole enlargement trends can be observed from linear fits to the caliper data with exposure time (Figure 2b). Enlargement over time is substantial in the upper section of Hole A and Hole B, which encounters the fault damage zone. However, the enlargement trend is not discernible in the lower portion of Hole A.

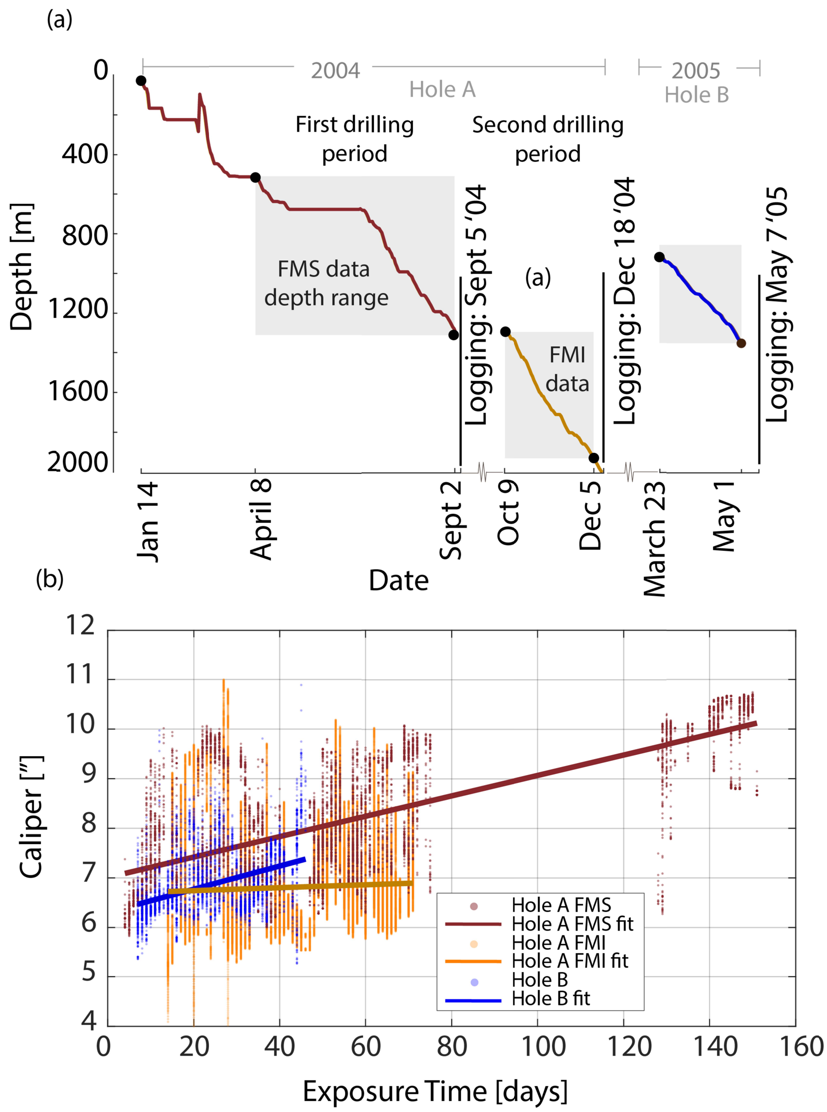

Figure 2. a) Depth of drilling plotted against the date of drilling. **b)** Caliper log data plotted with the exposure time of the borehole. Trends are shown for the upper and lower part of Hole A and the entire Hole B.

3.4 State of stress in the fault damage zone

We plot the near-continuous profile of pre-earthquake stress magnitudes prior to the 1999 Chi-Chi earthquake obtained from wellbore failure observations and edge dislocation modeling in Talukdar et al. (2022) (Figure 3a). We observe that the gradient of S_{Hmax} decreases at depths greater than 1000 m, as indicated in comparison with the dotted orange line showing a 55

MPa/km gradient. We also observe an increase in S_{hmin} with respect to the 12 MPa/km gradient line between 1080 and 1260 m. These changes in principal stress magnitudes between 1080 and 1260 m suggest lower differential stress magnitudes within the damage zone, especially compared to the hanging wall. The stress state along the borehole is also plotted in a normalized stress polygon in Figure 3b. The stress state along the entire borehole mostly falls within frictional limits set by a typical rock friction coefficient of 0.6-0.85 (Byerlee, 1978) (shown by gray dots), but the stress state in the Chelungpu fault damage zone (from 1080-1260 m) was closer to isotropic state where $S_{hmin} = S_{Hmax} = S_v$. This can be observed in the damage zone data points, which are color-coded by depth in Figure 3b. We plot histograms of the Von-Mises stress (normalized by vertical stress) of the damage zone and the host rock to also show that the stress state is more isotropic in the damage zone compared to the host rock (Figure 3b).

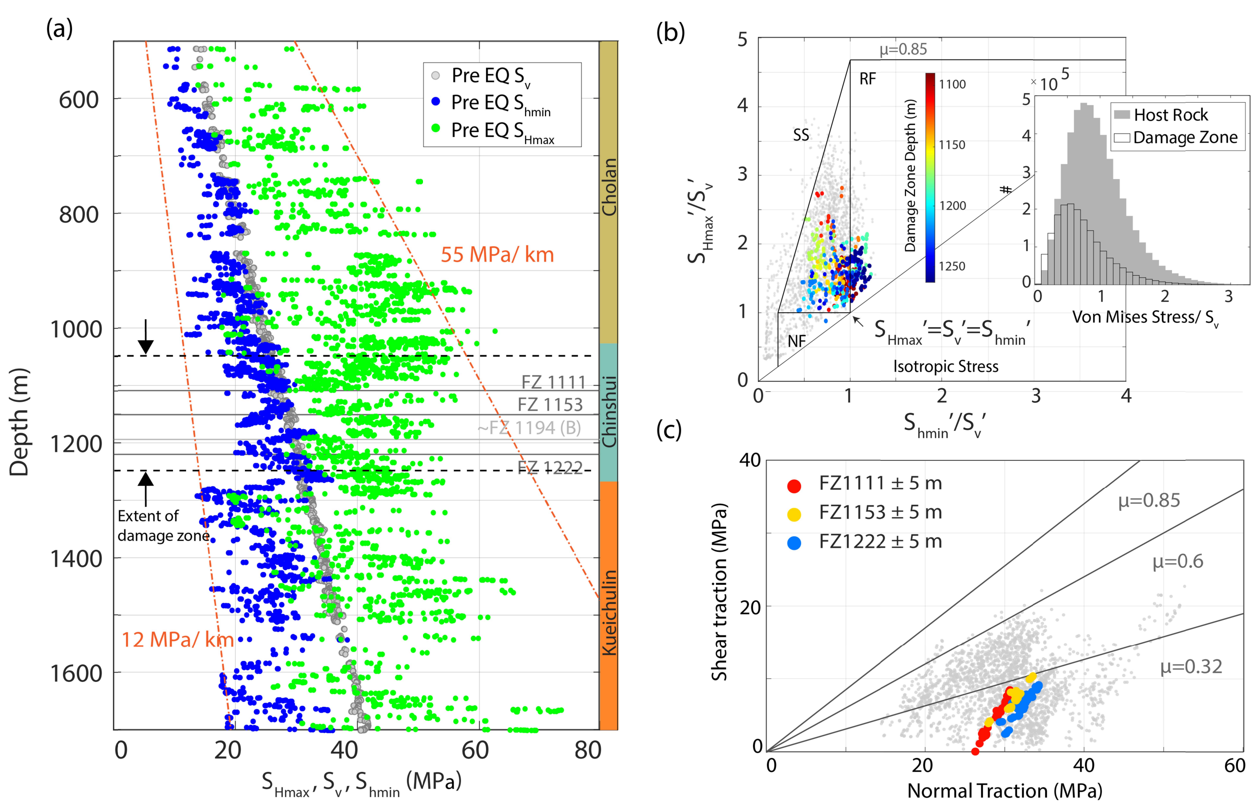

Figure 3. a) Pre-earthquake principal stress magnitudes S_{Hmax}, S_{hmin}, $S_{v,}$ and Pore fluid pressure (Pp) with depth. Two orange lines show a gradient of 12 MPa/km and 55 MPa/km. **b)** Plot of pre-earthquake effective horizontal stress normalized by pre-earthquake effective vertical stress. The damage zone data points are color-coded by depth. The inset shows histograms of Von Mises stress normalized by vertical stress for host rock and damage zone. **c)** Plot of shear vs. normal traction. Data within 5 m of the fault zones is highlighted. Lines correspond to typical Byerlee friction coefficients of 0.6 and 0.85, as well as experimentally measured frictional coefficient of TCDP gouge, i.e., 0.32, measured by Mizoguchi et al. (2008).

We used pre-earthquake stress magnitudes to calculate shear and normal traction resolved on fractures and secondary fault planes, which are dominantly parallel to the primary slip plane of the Chi-Chi earthquake as seen from core observations and image logs (Yeh et al., 2007). The ratio of shear stress to normal stress (i.e., the slip tendency) along the entire borehole is also within typical friction coefficients of 0.6 and 0.85 (Figure 3c), but the slip tendency is much lower in the damage zone within 5 meters of the fault cores. Slip tendency is even lower than the measured minimum frictional coefficient of fault gouge material (i.e., 0.32) recovered from Hole B fault zones (Mizoguchi et al., 2008).

3.5 Elastic model of damage zone stress

Damage zone stress state can approach an isotropic state due to the increase in microcrack density and the associated change in elastic stiffness approaching the fault core (Faulkner et al., 2006). Damage zones are suggested to have higher Poisson's ratio and lower Young's Modulus with increasing micro-fractures (Figure 4b), leading to a local rotation in principal stress and lower differential stress in the fault zone, *i.e.* a stress state closer to isotropic state. We evaluate if such local change in elastic properties in the fault zone is responsible for the locally isotropic stress state observed around the Chelungpu fault in TCDP. In TCDP, we observe a decrease in fracture density with distance from the fault core. Thus, we model the damage zone as fault parallel layers, each with a lower Poisson's ratio and higher Young's modulus with distance from the fault (Figure 4b). We use the multilayer model by Casey (1980) to calculate the change in magnitude and direction of principal stresses due to the damage-induced changes in elastic properties upon entering a layer with different elastic properties. This model assumes constant strain along the slip direction and traction equilibrium along the interface between layers:

$$\sigma_{yy} = \sigma_{yy}^{'} \tag{1}$$

$$\tau_{xy} = \tau_{xy}^{'} \tag{2}$$

$$\varepsilon_{xx} = \varepsilon_{xx}^{'} \tag{3}$$

where *x* and *y* are parallel and perpendicular, respectively, to a 30° dipping fault in an East-West vertical profile containing the dip direction. σ, τ and ε indicate normal stress, shear stress, and normal strain components, respectively within a layer. The apostrophe (‘) indicates the stress components in an adjacent layer.

Using the above boundary conditions (Equations 1, 2, and 3) and Hooke's Law, we can obtain σ, τ and ε magnitudes for the range of possible elastic properties contrast to calculate the corresponding possible range of S_{Hmax} and S_v in the fault-parallel layers (Figure 4c). The stress magnitude thus determined is dependent on Young's modulus ratio (R_E = Young's modulus of damage zone divided by Young's modulus of host rock), ratio of Poisson's ratio (R_v = Poisson's ratio of damage zone divided by Poisson's ratio of host rock) and the absolute magnitude of host rock Poisson's ratio (v_0). The stress magnitudes are independent of the absolute magnitude of Young's modulus.

We assumed a far-field stress magnitude of 50 MPa and 27 MPa for S_{Hmax} and S_v, respectively, based on our calculations of pre-earthquake in-situ stress magnitudes (Talukdar et al., 2022). The intermediate stress S_{hmin}, which obeys the plane strain boundary condition in this model, is not relevant to our discussion because it is the principal stress in the vertical plane spanned by the x and y axes that drive the dip-slip fault motion. Elastic properties are obtained from density and sonic logs. Poisson's ratio ranged from 0.25-0.35 whereas Young's Modulus ranged from 22 GPa to 32 GPa. These maximum and minimum values determine the range of R_E and R_v values considered in the calculation. The resultant stress magnitudes are plotted as four diamond polygons in Figure 4c, each corresponding to a different R_E. Higher R_E yields lower S_{Hmax} and S_v. Note that the maximum predicted deviation of the principal stress from the vertical direction due to the contrast in elastic property across the fault damage zone is generally less than 10° (Figure 4d) which would have a minimal effect when comparing the model results with stress magnitudes from breakout analysis (Peska and Zoback, 1995).

To find the difference in principal stress magnitudes in the multilayer model given by the range of elastic properties, we computed the ratio of maximum shear stress $((\sigma_1 - \sigma_2)/2)$ to mean stress $((\sigma_1 + \sigma_2)/2)$ (Figure 4e). Since the state of stress is perfectly isotropic when the ratio of maximum shear stress to mean stress is equal to 0, the magnitude of $(\sigma_1 - \sigma_2)/(\sigma_1 + \sigma_2)$ is a proxy for how much the stress state deviates from isotropic state. The magnitude of $(\sigma_1 - \sigma_2)/(\sigma_1 + \sigma_2)$ is lower at high Young's modulus ratio. We then compare the $(\sigma_1 - \sigma_2)/(\sigma_1 + \sigma_2)$ ratio calculated from the elastic multilayer model with the borehole observations. We find that the observed stress state in the damage zone is more isotropic than predicted from the elastic model.

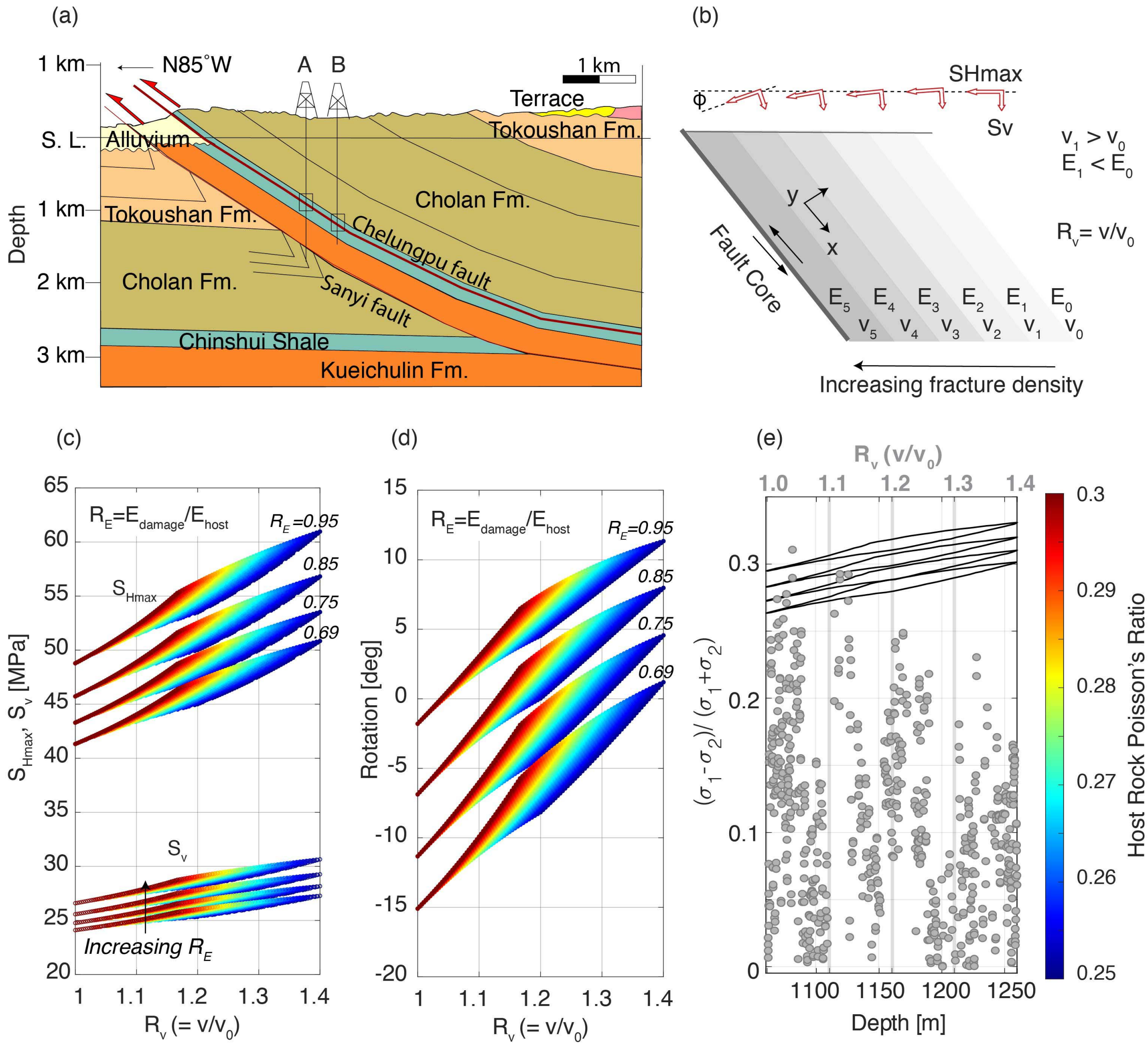

Figure 4. a) Vertical cross-section of the geology and structure around the TCDP drill site (Talukdar et al., 2022). **b)** Model schematic showing layers parallel to the fault with different elastic properties (not drawn to scale, number of layers arbitrary). ϕ is the angle of rotation of the principal stress due to elastic property contrast. **c)** Principal stress magnitudes calculated from the model for a set of Young's modulus ratios (R_E) and Poisson ratio contrast (R_v), color-coded by the host rock Poisson's ratio. **d)** Rotation angle of the principal stress from vertical direction plotted against Poisson's ratio contrast (R_v). **e)** Comparison

of the model (black parallelograms) and field data (gray circles) of the ratio of maximum shear stress to mean stress.

4 Discussion and Interpretation

4.1 Evidence of time-dependent deformational behavior

Although no significant difference in fracture density was observed between the three fault zones, pronounced sonic velocity reduction in the shallowest fault zone indicates lower stiffness and lower strength of the damage zone rocks. Previous studies show that the shallowest fault zone has the lowest resistivity (Wu et al., 2008), and the highest porosity and water content (Lin et al., 2008), indicating that there are more open and unhealed fractures in the damage zone of the shallowest fault (Figure 1). Therefore, we suggest that out of the three faults, the shallowest fault had a shorter time for healing and velocity recovery since the last rupture event. Orientation of the shallow seismic reflection (Wang 2002; Wang et al., 2002) and the ultra-fine-grained fault gouge found at 1111 m depth (Ma et al., 2006) have also suggested that the shallowest of the three faults is the youngest fault, which formed during the Chi-Chi earthquake. These observations indicate that healing and porosity reduction due to time-dependent deformation are taking place in the damage zone.

In the TCDP boreholes, a strong positive correlation of borehole diameter in the damage zone with exposure time also suggests that rock damage enhances time-dependent borehole enlargement (Figure 2b). Note that such a positive correlation was not observed outside of the damage zone in Hole A. Such time-dependent borehole enlargement can be caused by the diffusion of high mud pressure into the formation (Paul and Zoback, 2008). However, the difference between mud pressure and pore pressure in the TCDP borehole is considered to have been less than 1 MPa/km (Haimson et al., 2010; Hung et al., 2009). Therefore, pore pressure diffusion was not likely the cause of the time-dependent borehole enlargement in this setting. Instead, it is caused by time-dependent deformation and failure (i.e., tertiary creep) of the rock itself promoted by the fractures present in the rock. Laboratory experiments have suggested that rocks with damage exhibit time-dependent viscous rheology due to the closure and sliding of fractures at various scales (Meyer et al., 2021; Sone and Condon, 2017; Talukdar et al., 2021).

4.2 Viscous stress relaxation in the fault damage zone

While contrast in elastic properties across the damage zone can lead to relatively isotropic stress states with low differential stresses in the damage zone, the elastic model results show higher differential stress than field data when elastic properties of TCDP rocks are considered (Figure 4e). Shear traction resolved on Chelungpu fault planes was also lower than the measured frictional strength of the gouge material. Note that these are estimates of the stress state *before* the Chi-Chi earthquake. Therefore, unless the shear traction was released by a previous fault slip and the fault was never loaded again since then, the estimated in-situ shear traction appears to be unexpectedly low for such active fault zone systems before a major rupture event.

We propose that the inferred low pre-earthquake shear traction on the fault plane is a consequence of interseismic deformation and stress relaxation that results from the mesoscopically plastic nature of highly fractured rocks in the damage zone. It has been shown in Barnett shale, Fort Worth Basin, that laboratory-measured creep properties of the shales correlate with the in-situ stress variations (Sone and Zoback, 2014a, b) suggesting the occurrence of viscous stress relaxation as predicted from standard viscoelastic theories (Lakes, 2009). Observations of fault healing and time-dependent borehole enlargement discussed above are all indicative of the slow time-dependent deformation that occurs within the damage zone. Such time-dependent deformation may locally reduce the differential stress in fault damage zones which is consistent with our observations.

5 Conclusions

We identified the damage zone of the Chelungpu fault system between 1080-1260 m depth as a broad region of enhanced fracture density, within which locally high fracture densities occur around the three main fault strands. The damage zone section not only shows evidence of local borehole enlargement but also time-dependent borehole enlargement. The fault plane that ruptured during the most recent earthquake is associated with the most prominent velocity reduction reflecting the shorter time for fault healing compared to the older fault strands. These observations are indicative of the time-dependent deformation occurring in the damage zone.

The in-situ stress state analyzed along the borehole also shows that the stress state is relatively isotropic and differential stress magnitude is low in the damage zone compared to the surrounding host rock. The locally diminished differential stress cannot be explained by a local perturbation in the stress state caused by the compromised elastic stiffness in the damage zone. Because of the co-occurrence of this stress anomaly and the interval exhibiting time-dependent deformation, we suggest that the low differential stress is caused by the long-term stress relaxation that occurred because of the time-dependent plastic rheology of fault damage zone rocks. Our results emphasize the need for quantifying the viscous rheology of fault damage zones and its importance in interpreting fault zone stress states.

Acknowledgments

This study was supported by National Science Foundation Award No. EAR1727661.

Open Research

We are in the process of uploading the borehole log data to the Minds@UW repository. Meanwhile, the data can also be found in the attached excel file named 'Log&StressData_GRL.'

References

Bird, P. (2009). Long-term fault slip rates, distributed deformation rates, and forecast of seismicity in the western United States from joint fitting of community geologic, geodetic, and stress direction data sets. *Journal of Geophysical Research: Solid Earth*, *114*(B11).

Byerlee, J. (1978). Friction of rocks. *Pure and Applied Geophysics PAGEOPH*. https://doi.org/10.1007/BF00876528

Casey, M. (1980). Mechanics of shear zones in isotropic dilatant materials. *Journal of Structural Geology*, *2*(1–2), 143–147.

Chester, F M, and Logan, J. M. (1986). Implications for mechanical properties of brittle faults from observations of the Punchbowl fault zone, California. *Pure and Applied Geophysics*, *124*(1), 79–106.

Chester, Frederick M, Evans, J. P., and Biegel, R. L. (1993). Internal structure and weakening mechanisms of the San Andreas fault. *Journal of Geophysical Research: Solid Earth*, *98*(B1), 771–786.

Cornet, F. H., Bérard, T., and Bourouis, S. (2007). How close to failure is a granite rock mass at a 5 km depth? *International Journal of Rock Mechanics and Mining Sciences*, *44*(1), 47–66.

Crouch, S. L., Starfield, A. M., and Rizzo, F. J. (1983). Boundary element methods in solid mechanics.

Faulkner, D. R., Mitchell, T. M., Healy, D., and Heap, M. J. (2006). Slip on'weak'faults by the rotation of regional stress in the fracture damage zone. *Nature*, *444*(7121), 922–925.

Fialko, Y. (2006). Interseismic strain accumulation and the earthquake potential on the southern San Andreas fault system. *Nature*, *441*(7096), 968–971.

Griffith, W.A., Sanz, P.F. and Pollard, D.D., (2009). Influence of outcrop scale fractures on the effective stiffness of fault damage zone rocks. *Pure and Applied Geophysics*, 166, pp.1595-1627.

Haimson, B., Lin, W., Oku, H., Hung, J. H., and Song, S. R. (2010). Integrating borehole-breakout dimensions, strength criteria, and leak-off test results, to constrain the state of stress across the Chelungpu Fault, Taiwan. *Tectonophysics*, *482*(1–4), 65–72. https://doi.org/10.1016/j.tecto.2009.05.016

Hirono, T., Yeh, E.-C., Lin, W., Sone, H., Mishima, T., Soh, W., et al. (2007). Nondestructive continuous physical property measurements of core samples recovered from hole B, Taiwan Chelungpu-Fault Drilling Project. *Journal of Geophysical Research: Solid Earth*, *112*(B7).

Hung, J. H., Ma, K. F., Wang, C. Y., Ito, H., Lin, W., and Yeh, E. C. (2009). Subsurface structure, physical properties, fault-zone characteristics and stress state in scientific drill holes of Taiwan Chelungpu Fault Drilling Project. *Tectonophysics*. https://doi.org/10.1016/j.tecto.2007.11.014

Johnson, K. M. (2013). Slip rates and off-fault deformation in Southern California inferred from GPS data and models. *Journal of Geophysical Research: Solid Earth*, *118*(10), 5643–5664.

Lakes, R. (2017). Viscoelastic Solids. *CRC Press.*

Li, H., Wang, H., Xu, Z., Si, J., Pei, J., Li, T., et al. (2013). Characteristics of the fault-related rocks, fault zones and the principal slip zone in the Wenchuan Earthquake Fault Scientific Drilling Project Hole-1 (WFSD-1). *Tectonophysics*, *584*, 23–42.

Lin, A., Maruyama, T., and Kobayashi, K. (2007). Tectonic implications of damage zone-related fault-fracture networks revealed in drill core through the Nojima fault, Japan. *Tectonophysics*, *443*(3–4), 161–173.

Lin, W., Matsubayashi, O., Yeh, E.C., Hirono, T., Tanikawa, W., Soh, W., Wang, C.Y., Song, S.R. and Murayama, M., (2008). Profiles of volumetric water content in fault zones retrieved from hole B of the Taiwan Chelungpu-Fault Drilling Project (TCDP). *Geophysical Research Letters*, *35*(1).

Lindsey, E. O., Sahakian, V. J., Fialko, Y., Bock, Y., Barbot, S., and Rockwell, T. K. (2014). Interseismic strain localization in the San Jacinto fault zone. *Pure and Applied Geophysics*, *171*(11), 2937–2954.

Ma, K.-F., Tanaka, H., Song, S.-R., Wang, C.-Y., Hung, J.-H., Tsai, Y.-B., et al. (2006). Slip zone and energetics of a large earthquake from the Taiwan Chelungpu-fault Drilling Project. *Nature*, *444*(7118), 473–476.

Ma, S. (2009). Distinct asymmetry in rupture-induced inelastic strain across dipping faults: An off-fault yielding model. *Geophysical Research Letters*, *36*(20).

Mastin, L. G. (1984). *The development of borehole breakouts in sandstone*. Stanford University, California.

Materna, K., and Bürgmann, R. (2016). Contrasts in compliant fault zone properties inferred from geodetic measurements in the San Francisco Bay area. *Journal of Geophysical Research: Solid Earth*, *121*(9), 6916–6931.

Meyer, G. G., Brantut, N., Mitchell, T. M., Meredith, P. G., and Plümper, O. (2021). Time dependent mechanical crack closure as a potential rapid source of post-seismic wave speed recovery: Insights from experiments in Carrara Marble. *Journal of Geophysical Research: Solid Earth*, *126*(4), e2020JB021301.

Mizoguchi, K., Takahashi, M., Tanikawa, W., Masuda, K., Song, S.R. and Soh, W., 2008. Frictional strength of fault gouge in Taiwan Chelungpu fault obtained from TCDP Hole B. *Tectonophysics*, *460*(1-4), pp.198-205.

Moore, J. C., Chang, C., McNeill, L., Thu, M. K., Yamada, Y., and Huftile, G. (2011). Growth of borehole breakouts with time after drilling: Implications for state of stress, NanTroSEIZE transect, SW Japan. *Geochemistry, Geophysics, Geosystems*, *12*(4).

Paul, P., and Zoback, M. (2008). Wellbore-stability study for the SAFOD borehole through the San Andreas Fault. *SPE Drilling \and Completion*, *23*(04), 394–408.

Peska, P., & Zoback, M. (1995). Observations of borehole breakouts and tensile wall-fractures in deviated boreholes: A technique to constrain in situ stress and rock strength. *35th U.S. Symposium on Rock Mechanics (USRMS), Reno, Nevada.*

Plumb, R. A., & Hickman, S. H. (1985). Stress-induced borehole elongation: A comparison between the four-arm dipmeter and the borehole televiewer in the Auburn Geothermal Well. *Journal of Geophysical Research: Solid Earth*, *90*(B7), 5513–5521. https://doi.org/10.1029/JB090iB07p05513

Sahara, D. P., Schoenball, M., Kohl, T., and Müller, B. I. R. (2014). Impact of fracture networks on borehole breakout heterogeneities in crystalline rock. *International Journal of Rock Mechanics and Mining Sciences*, *71*, 301–309.

Scholz, C. H. (2019). *The mechanics of earthquakes and faulting*. Cambridge university press.

Shipton, Z. K., and Cowie, P. A. (2001). Damage zone and slip-surface evolution over \$µ\$m to km scales in high-porosity Navajo sandstone, Utah. *Journal of Structural Geology*, *23*(12), 1825–1844.

Sibson; H. R. (2003). Thickness of the Seismic Slip Zone. Bulletin of the Seismological Society of America. 93 (3): 1169–1178. doi: https://doi.org/10.1785/0120020061

Sone, H, Condon, K. J., and others. (2017). Ductile behavior of thermally-fractured granite rocks. In *51st US Rock Mechanics/Geomechanics Symposium*.

Sone, H., and Uchide, T. (2016). Spatiotemporal evolution of a fault shear stress patch due to viscoelastic interseismic fault zone rheology. *Tectonophysics*. https://doi.org/10.1016/j.tecto.2016.04.017

Sone, H., & Zoback, M. D. (2014a). Time-dependent deformation of shale gas reservoir rocks and its long-term effect on the in situ state of stress. *International Journal of Rock Mechanics and Mining Sciences*, *69*, 120–132. https://doi.org/10.1016/j.ijrmms.2014.04.002

Sone, H., & Zoback, M. D. (2014b). Viscous relaxation model for predicting least principal stress magnitudes in sedimentary rocks. *Journal of Petroleum Science and Engineering*, *124*, 416–431. https://doi.org/10.1016/j.petrol.2014.09.022

Sone, H., Yeh, E.-C., Nakaya, T., Ji-Hao, H., Kuo-Fong, M., Chien-Ying, W., et al. (2007). Mesoscopic structural observations of cores from the Chelungpu fault system, Taiwan Chelungpu-fault Drilling Project Hole-A, Taiwan. *TAO: Terrestrial, Atmospheric and Oceanic Sciences*, *18*(2), 359.

Song, S. R., Kuo, L. W., Yeh, E. C., Wang, C. Y., Hung, J. H., & Ma, K. F. (2007). Characteristics of the lithology, fault-related rocks and fault zone structures in TCDP Hole-A. *Terrestrial, Atmospheric and Oceanic Sciences*, 18(2), 243.

Talukdar, M, Sone, H., and Griffith, W. A. (2021, June 18). Viscoplastic Modeling of Elastic and Creep Deformation of Fractured Berea Sandstone. *55th U.S. Rock Mechanics/Geomechanics Symposium*.

Talukdar, M., Sone, H. and Kuo, L.W., (2022). Lithology and Fault-Related Stress Variations Along the TCDP Boreholes: The Stress State Before and After the 1999 Chi-Chi Earthquake. *Journal of Geophysical Research: Solid Earth*, *127*(2), p.e2021JB023290.

Wang, C.Y., (2002). Detection of a recent earthquake fault by the shallow reflection seismic method. *Geophysics*, *67*(5), pp.1465-1473.

Wang, C.Y., Li, C.L. and Yen, H.Y., (2002). Mapping the northern portion of the Chelungpu fault, Taiwan by shallow reflection seismics. *Geophysical Research Letters*, *29*(16), pp.37-1.

Wu, Y.H., Yeh, E.C., Dong, J.J., Kuo, L.W., Hsu, J.Y. and Hung, J.H., (2008). Core-log integration studies in hole-A of Taiwan Chelungpu-fault Drilling Project. *Geophysical Journal International*, *174*(3), pp.949-965.

Yeh, E. C., Sone, H., Nakaya, T., Ian, K. H., Song, S. R., Hung, J. H., et al. (2007). Core description and characteristics of fault zones from Hole-A of the Taiwan Chelungpu-Fault Drilling Project. *Terrestrial, Atmospheric and Oceanic Sciences*. https://doi.org/10.3319/TAO.2007.18.2.327(TCDP)

Zoback, M. D., Moos, D., Mastin, L., and Anderson, R. N. (1985). Well bore breakouts and in situ stress. *Journal of Geophysical Research: Solid Earth*, *90*(B7), 5523–5530.

Figure 1.

(a)
(b)
(c)
(d)
Depth in Hole A (m)
Cholan
Chinshui
Kueichulin
Data
Moving Average
Extent of damage zone
FZ 1111
FZ 1153
FZ 1222
~FZ 1134
~FZ 1194
~FZ 1243
FMS Caliper 1
FMS Caliper 2
FMI Caliper 1
FMI Caliper 2
Bit size
Hole A Fracture Density (#/m)
Hole B Fracture Density (#/m)
Hole A Caliper (inch)
Hole B Caliper (inch)
Hole A Caliper diff (inch)
Hole B Caliper diff (inch)
P wave velocity (km/s)
S wave velocity (km/s)

Figure 2.

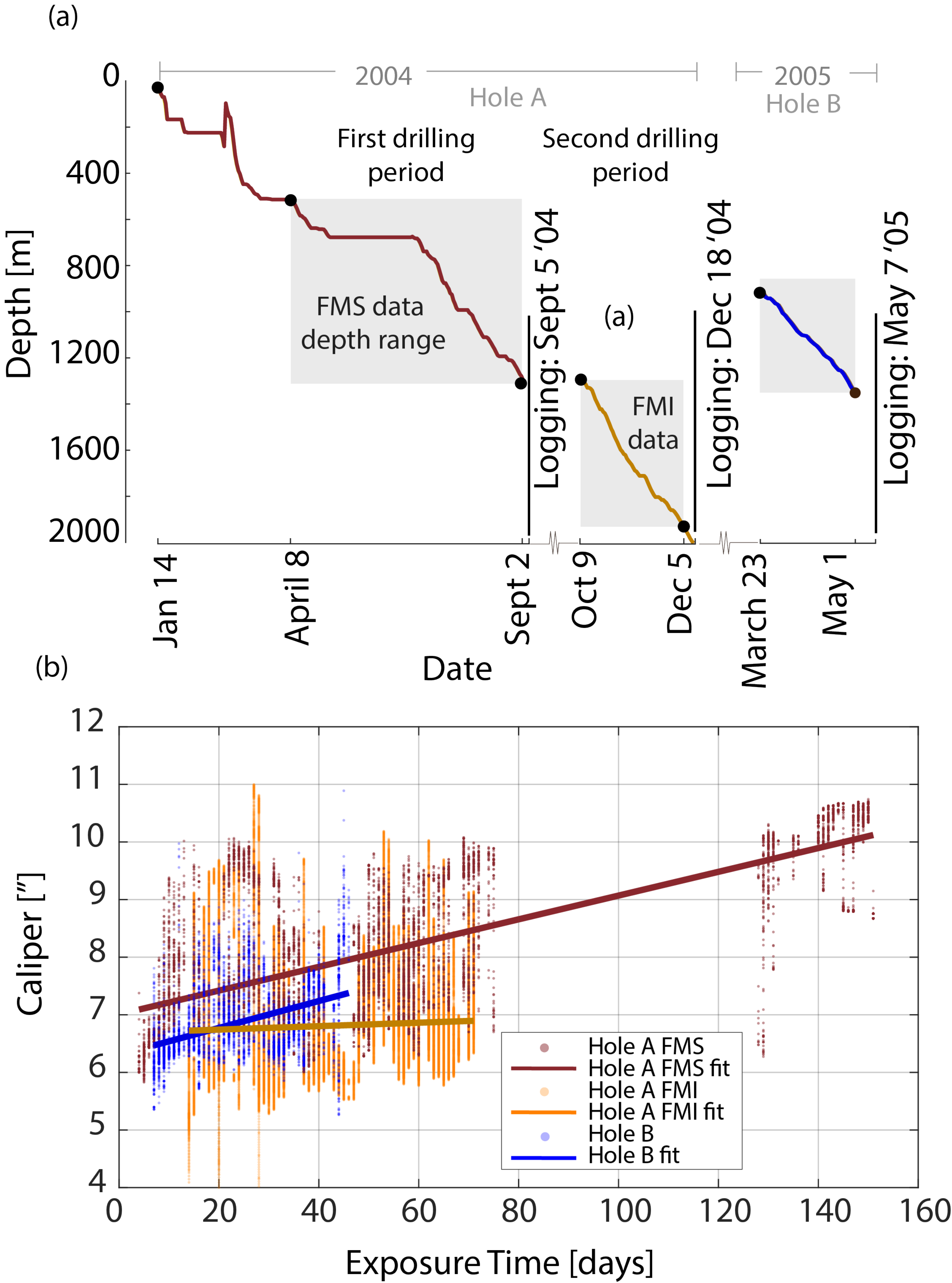

(a)
2004
Hole A
2005
Hole B
First drilling period
Second drilling period
FMS data depth range
FMI data
(a)
Logging: Sept 5 '04
Logging: Dec 18 '04
Logging: May 7 '05
Depth [m]
0
400
800
1200
1600
2000
Jan 14
April 8
Sept 2
Oct 9
Dec 5
March 23
May 1
Date
(b)
Caliper ["]
Exposure Time [days]
Hole A FMS
Hole A FMS fit
Hole A FMI
Hole A FMI fit
Hole B
Hole B fit

Figure 3.

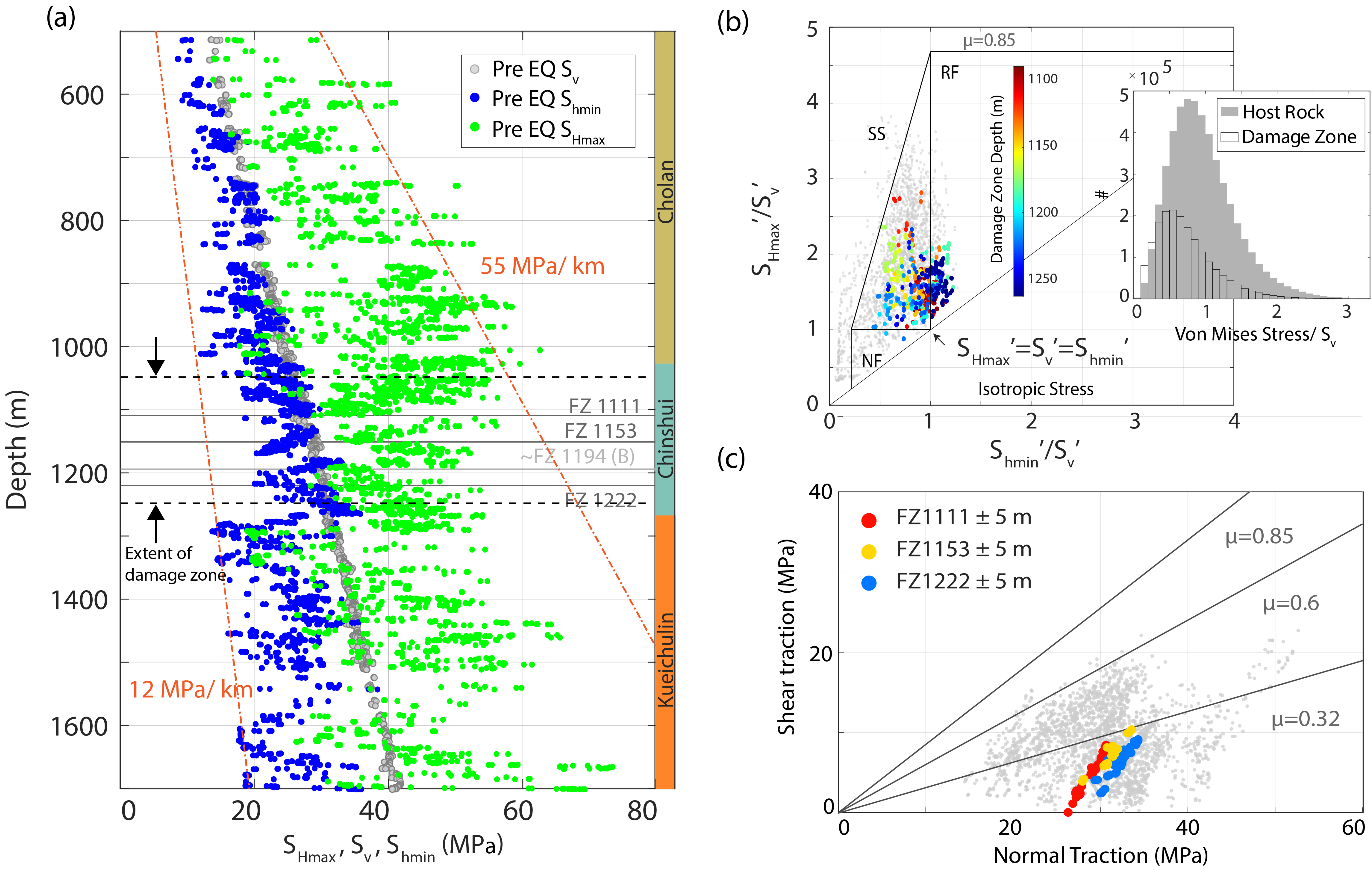

(a)
Depth (m)
600
800
1000
1200
1400
1600
0
20
40
60
80
S_{Hmax}, S_v, S_{hmin} (MPa)
Pre EQ S_v
Pre EQ S_{hmin}
Pre EQ S_{Hmax}
55 MPa/ km
12 MPa/ km
FZ 1111
FZ 1153
~FZ 1194 (B)
FZ 1222
Extent of
damage zone
Cholan
Chinshui
Kueichulin
(b)
S_{Hmax}'/S_v'
S_{hmin}'/S_v'
μ=0.85
RF
SS
NF
Damage Zone Depth (m)
1100
1150
1200
1250
$S_{Hmax}'=S_v'=S_{hmin}'$
Isotropic Stress
$\times 10^5$
#
Host Rock
Damage Zone
Von Mises Stress/ S_v
(c)
Shear traction (MPa)
Normal Traction (MPa)
FZ1111 ± 5 m
FZ1153 ± 5 m
FZ1222 ± 5 m
μ=0.85
μ=0.6
μ=0.32

Figure 4.

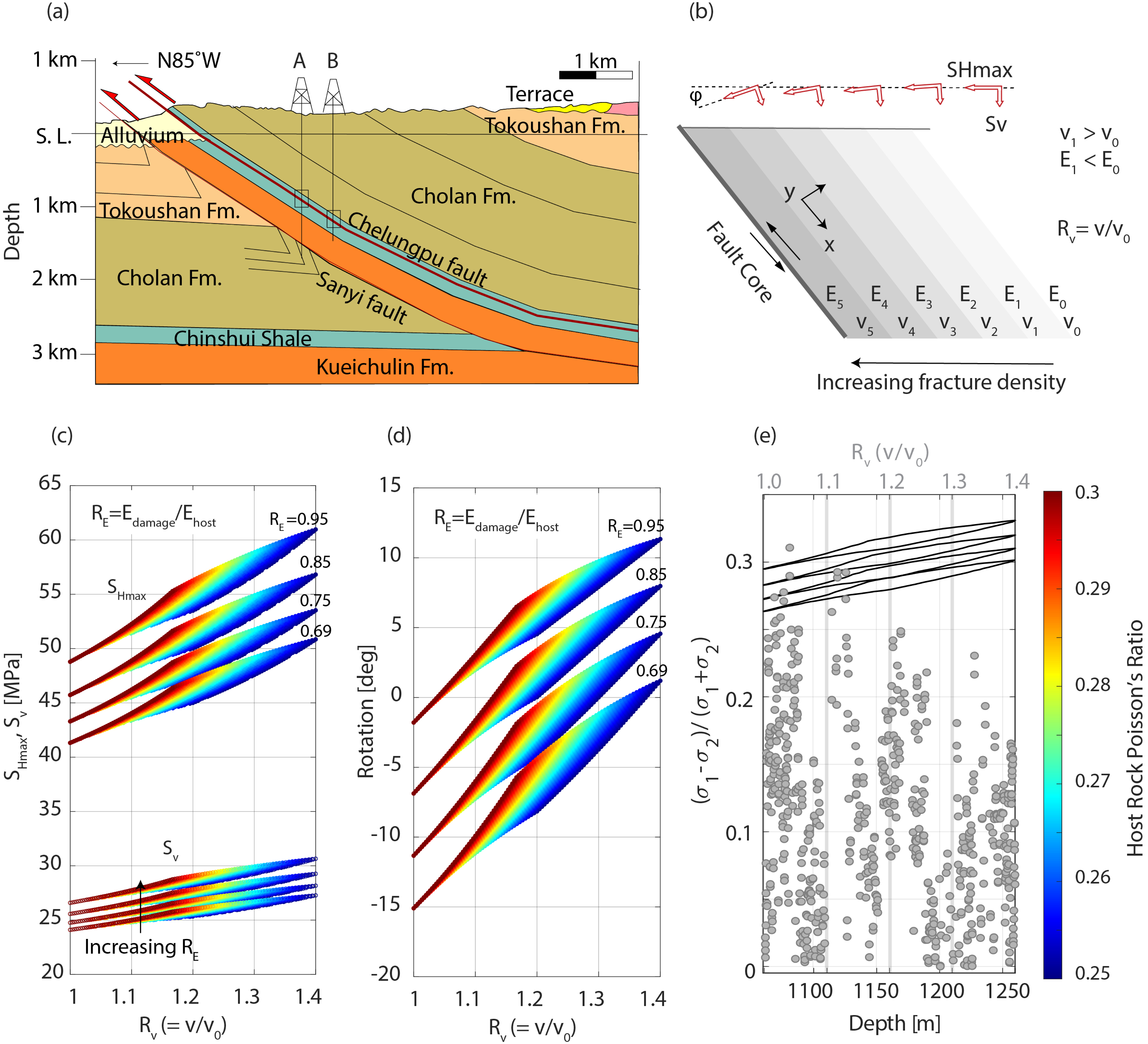

(a)
1 km
N85°W
A
B
1 km
Terrace
Tokoushan Fm.
S. L.
Alluvium
1 km
Tokoushan Fm.
Cholan Fm.
Chelungpu fault
Depth
2 km
Cholan Fm.
Sanyi fault
Chinshui Shale
3 km
Kueichulin Fm.
(b)
SHmax
φ
Sv
$v_1 > v_0$
$E_1 < E_0$
y
x
$R_v = v/v_0$
Fault Core
E_5 E_4 E_3 E_2 E_1 E_0
v_5 v_4 v_3 v_2 v_1 v_0
Increasing fracture density
(c)
$R_E = E_{damage}/E_{host}$
$R_E = 0.95$
0.85
0.75
0.69
S_{Hmax}
S_v
Increasing R_E
S_{Hmax}, S_v [MPa]
$R_v (= v/v_0)$
(d)
$R_E = E_{damage}/E_{host}$
$R_E = 0.95$
0.85
0.75
0.69
Rotation [deg]
$R_v (= v/v_0)$
(e)
$R_v (v/v_0)$
$(\sigma_1 - \sigma_2)/(\sigma_1 + \sigma_2)$
Depth [m]
Host Rock Poisson's Ratio